



UvA-DARE (Digital Academic Repository)

Contribution of the Core to the Thermal Evolution of Sub-Neptunes

Vazan, A.; Ormel, C.W.; Noack, L.; Dominik, C.

DOI

[10.3847/1538-4357/aaef33](https://doi.org/10.3847/1538-4357/aaef33)

Publication date

2018

Document Version

Final published version

Published in

Astrophysical Journal

[Link to publication](#)

Citation for published version (APA):

Vazan, A., Ormel, C. W., Noack, L., & Dominik, C. (2018). Contribution of the Core to the Thermal Evolution of Sub-Neptunes. *Astrophysical Journal*, *869*(2), [163].
<https://doi.org/10.3847/1538-4357/aaef33>

General rights



It is not permitted to download or to forward/distribute the text or part of it without the consent of the author(s) and/or copyright holder(s), other than for strictly personal, individual use, unless the work is under an open content license (like Creative Commons).

Disclaimer/Complaints regulations

If you believe that digital publication of certain material infringes any of your rights or (privacy) interests, please let the Library know, stating your reasons. In case of a legitimate complaint, the Library will make the material inaccessible and/or remove it from the website. Please Ask the Library: <https://uba.uva.nl/en/contact>, or a letter to: Library of the University of Amsterdam, Secretariat, Singel 425, 1012 WP Amsterdam, The Netherlands. You will be contacted as soon as possible.



Contribution of the Core to the Thermal Evolution of Sub-Neptunes

A. Vazan¹ , C. W. Ormel¹, L. Noack², and C. Dominik¹ 

¹ Astronomical Institute Anton Pannekoek, University of Amsterdam, The Netherlands; a.vazan@uva.nl

² Department of Earth Sciences, Institute of Geological Sciences, FU Berlin, Germany

Received 2018 September 5; revised 2018 November 4; accepted 2018 November 5; published 2018 December 21

Abstract

Sub-Neptune planets are a very common type of planet. They are inferred to harbor a primordial (H/He) envelope on top of a (rocky) core, which dominates the mass. Here, we investigate the long-term consequences of the core properties on the planet mass–radius relation. We consider the role of various core energy sources resulting from core formation, its differentiation, its solidification (latent heat), core contraction, and radioactive decay. We divide the evolution of the rocky core into three phases: the formation phase, which sets the initial conditions, the magma ocean phase, characterized by rapid heat transport, and the solid-state phase, where cooling is inefficient. We find that for typical sub-Neptune planets of $\sim 2\text{--}10 M_{\oplus}$ and envelope mass fractions of 0.5%–10%, the magma ocean phase lasts several gigayears, much longer than for terrestrial planets. The magma ocean phase effectively erases any signs of the initial core thermodynamic state. After solidification, the reduced heat flux from the rocky core causes a significant drop in the rocky core surface temperature, but its effect on the planet radius is limited. In the long run, radioactive heating is the most significant core energy source in our model. Overall, the long-term radius uncertainty by core thermal effects is up to 15%.

Key words: methods: numerical – planets and satellites: composition – planets and satellites: interiors – planets and satellites: physical evolution

1. Introduction

Exoplanets in the range of several Earth masses are very common in our galaxy (Howard et al. 2012; Batalha et al. 2013; Coughlin et al. 2016). The observed mass–radius relation for some of these planets suggest that some are bare rocky planets with no envelope, and some are inferred to contain some amount of hydrogen and helium (sub-Neptunes) on top of a rock/iron core (hereafter core). The inferred envelope masses for sub-Neptunes are typically of several percent (Lopez et al. 2012; Wolfgang & Lopez 2015; Jontof-Hutter et al. 2016), i.e., most of the planet mass is in the core. In such a planet, the core can perform as an energy reservoir for the envelope.

In contrast to envelope (gases) cooling and contraction, the core radius is not expected to change much during the planetary evolution (Rogers & Seager 2010). However, the heat flux from the core can affect the thermal properties of the low-mass envelope by heating it from below. High-enough heat flux from the core can lead to envelope mass loss (Ginzburg et al. 2016, 2018), but even a moderate flux from the core can change the envelope thermal properties. Hence, the thermal evolution of the core indirectly affects the planet radius.

Previous astrophysical studies have accounted for some of the core properties, like the decay of radioactive materials, when modeling the thermal evolution of the envelope (e.g., Lopez & Fortney 2014; Howe & Burrows 2015; Chen & Rogers 2016), assuming an isothermal core that cools in the cooling rate of the envelope. However, in the mass range of Neptune-like planets, the core thermal properties can be significant (Baraffe et al. 2008). A key factor in the core–envelope thermal evolution is thus the timescale on which the core releases its heat; if the cooling is on a gigayear timescale, the observed radius is affected by it (Vazan et al. 2018). In order to study the timescale for the core cooling, its thermal evolution should be modeled explicitly.

In geophysical studies, core heat transport is explicitly modeled (Turcotte & Oxburgh 1967; Stevenson et al. 1983). The cooling rate is determined by the properties of high-viscosity convection and the resulting conductive boundary layers between convective regions. In these models, the surface temperature of the planet is fixed as there is no thick envelope. By contrast, in the case of sub-Neptune planets, the surface temperature changes in time due to the envelope’s cooling and contraction. The thick, gaseous envelope keeps the temperature (and the pressure) at the core surface higher than in an Earth-like case, affecting the viscosity and the state of the core (solid/liquid). Thus, for sub-Neptunes the heat transport properties of the core depend on the envelope properties. Therefore, both envelope and core should be modeled simultaneously.

In this work, we model the thermal evolution of the planet as a whole, center to surface, and study the effects of the underlying thermal parameters on the state of the core and on the derived planet radius. In Section 2, we discuss our model and define the different phases of the core thermal evolution. In Section 3, we show our results for sub-Neptune planets of $\sim 2\text{--}10 M_{\oplus}$ with envelope mass fractions of 0.1%–20% and examine thermal properties that lie within the uncertainty of geophysical models. We discuss the sub-Neptunes thermal evolution perspective in Section 4 and draw our conclusions in Section 5.

2. The Model

We calculate the thermal evolution of sub-Neptune planets with a rocky core and a hydrogen–helium envelope on a single structure grid (see Section 2.4). As illustrated in Figure 1, we divide the evolution of the planet into three phases:

1. Formation—the conditions of the core and the gaseous envelope as derived from estimates of core formation (see Section 2.1).

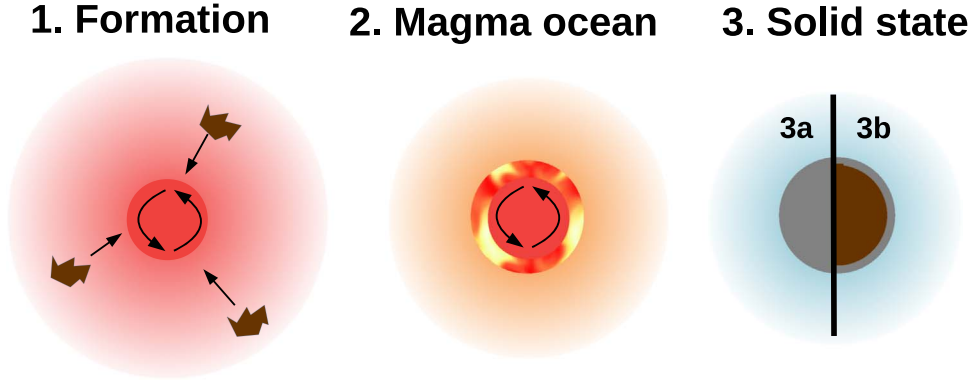


Figure 1. The three phases of the core evolution. 1. Formation—the core is hot due to the conversion of binding energy to heat. 2. Magma ocean phases—vigorous (liquid) core convection. 3. Solid state—we consider either an entirely conductive core (3a) or a convective core with a conductive core surface (3b).

2. Magma ocean—vigorous (liquid) core convection and efficient heat transport from the core to the gaseous envelope.
3. Solid state—solidification of the core surface and conductive (reduced) heat transfer from the core to the envelope.

The formation phase, in which the planet assembles in the presence of a gas-rich disk, is not explicitly modeled, but provides the initial conditions for the subsequent disk-free phases. The transition from phase 2 to phase 3 occurs when the core surface temperature drops below the solidification temperature for the surface pressure (see Section 2.2). This transition is approximated to be instantaneous. The timing of the transition depends on the cooling of the core and the envelope, and on the core energy sources (see Section 2.3). After solidification (phase 3), core heat transport slows down significantly. We distinguish two end-member scenarios: (3a) conductive core and (3b) convective core with conductive surface boundary layer.

In contrast to previous works, we determine the core thermal evolution from the perspective of the core thermal properties and not from the envelope evolution. The change in core properties in time is simulated by the three phases. The evolution path is continuous between the phases: at the end of each phase, the structural parameters (radius, temperature, density, luminosity, and composition for each mass layer) are being used for the first step of the next phase.

2.1. Initial Conditions

The initial energy content of the planet is determined by its formation. During the formation of a core, the gravitational energy from the accumulation of the solid materials partially transforms to thermal energy. The speed of the accumulation process, as well as the material properties, determine which fraction of the gravitational binding energy is locked up in the planet in the form of thermal energy. A fast-forming core may retain large fraction of the initial binding energy and reach high initial temperatures. On the other hand, for a slow core formation, a substantial amount of the binding energy is released already during the formation process (by radiation), which results in lower initial temperatures.

The maximal temperature for the core formation can be estimated from the gravitational binding energy:

$$E_{\text{binding}} = \frac{3GM_c^2}{5R_c}. \quad (1)$$

The maximal temperature is achieved when all the binding energy is converted to heat, i.e., $E_{\text{binding}} = C_p M_c T_{\text{max}}$, and thus

$$T_{\text{max}} \sim \frac{GM_c}{R_c C_p} = 4.8 \times 10^4 \text{ K} \left(\frac{M_c}{1 M_{\oplus}} \right) \times \left(\frac{R_c}{1 R_{\oplus}} \right)^{-1} \left(\frac{C_p}{1 \text{ kJ}(\text{kg K})^{-1}} \right)^{-1}, \quad (2)$$

where M_c and R_c are the core mass and radius, G is the gravitational constant, and C_p is rock heat capacity (Guillot et al. 1995). For a $4.5 M_{\oplus}$ rocky planet of $1.65 R_{\oplus}$, we get $T_{\text{max}} = 1.3 \times 10^5 \text{ K}$. This is rather high, since it assumes no radiative or advective losses. But even when the initial temperature will be a fraction of T_{max} , a substantial amount of heat is locked in the core, and the rocky part will radiate at a high luminosity. Since the fraction of gravitational binding energy that is left in the core after formation is unknown, we consider here a wide range of fractions between 5% and 50% of E_{binding} .

The core is embedded in an initially diluted adiabatic envelope. We assume that the planet envelope is formed by gas accretion during the disk phase (Pollack et al. 1996; Ikoma & Hori 2012) and therefore is composed of hydrogen and helium at solar ratio. The envelope extends initially to the planet Hill radius.³

2.2. Flux from the Core

Heat transport by convection in the core is determined by the Rayleigh number,

$$Ra = \frac{\rho \alpha g \Delta T D^3}{\kappa \eta}, \quad (3)$$

which depends not only on structure properties such as gravity (g), density (ρ), layer thickness (D), and the temperature difference within the layer (ΔT), but also on material properties such as the thermal expansion coefficient (α), thermal diffusivity (κ), and kinematic viscosity (η). Convection occurs for Rayleigh numbers greater than a critical value (here we use $Ra_{\text{crit}} = 450$; Morschhauser et al. 2011). According to Equation (3), convection is less likely and less vigorous if

³ We also calculated using the initial radius of $0.1 R_{\text{Hill}}$ and find a very minor effect on the long-term evolution for all cases.

viscosity η and thermal conductivity κ are high. Between these two, the viscosity is the key factor in regulating the convection, since it is an exponential function of the local physical conditions. Specifically, we approximated the viscosity by (e.g., Karato & Wu 1993; Poirier 2000; Noack et al. 2016)⁴

$$\eta(T) = \eta_0 \exp \left[\frac{E_0}{R_g} \left(\frac{1}{T} - \frac{1}{T_0} \right) \right], \quad (4)$$

where reference values are extrapolated from an Earth-like composition: viscosity $\eta_0 = 10^{21}$ Pa s, temperature $T_0 = 1600$ K, and activation energy $E_0 = 240$ kJ mol⁻¹; R_g is the gas constant.

In the core–envelope boundary (hereafter CEB), heat is transported by conduction. The thickness of the conductive layer δ is determined by the vigor of the underlying convection (Stevenson et al. 1983),

$$\delta = D \left(\frac{Ra_{\text{crit}}}{Ra} \right)^{1/3}. \quad (5)$$

As the core cools and the viscosity increases, the Rayleigh number is lower and thus the conductive boundary layer becomes thicker. Since heat transport in the boundary layer operates by conduction—a diffusive process—core cooling depends on the conductive timescale, which is on the order of $\tau_{\text{cond}} = \delta^2/\kappa$.

Initially, the core is in a magma ocean phase—a fluid phase of very low viscosity—due to its high temperature from formation. In this phase, the conductive boundary layer is very thin and thus the conductive timescale is short ($\tau_{\text{cond}} \leq 10^6$ yr). In this phase, we assume efficient heat transport from the core to the envelope and in the core, i.e., we simply ignore the conductive CEB and model the core as adiabatic.

The magma ocean phase continues until at some point the core is cold enough to allow solidification of the core surface. To find this point, we compare the CEB temperature with the critical melting temperature for the Earth mantle composition, as described in Appendix A.1. The magma ocean solidifies from the bottom upward, since the melting temperature of rock increases more strongly with pressure than the increase in temperature of the adiabatic core structure. Therefore, CEB solidification implies that the core can no longer be modeled by low-viscosity convection.

After solidification, the high viscosity of the rock slows down heat transport in the core. The change in the core heat transport after solidification is a gradual process, which depends on uncertain structure and material properties.⁵ For simplicity, we consider here two extreme limits:

- a conductive core, where we assume that convection will be suppressed due to the high interior pressure (e.g., van den Berg et al. 2010; Stamenković et al. 2012), and
- a convecting core, with a conductive thermal CEB layer (including the crust) on top of it.

⁴ In high pressure scenarios such as that in the inner part of sub-Neptunes, viscosity also strongly depends on pressure (Stamenković et al. 2011; Tackley et al. 2013). Here we neglect the pressure term in the viscosity equation, because we focus on the conditions at the core–envelope boundary, where the pressure is not more than several GPa for a sub-Neptune mass range. This may slightly overestimate the cooling of the core.

⁵ Solidification also depends on the exact rock composition; very different compositions can lead to different solidification temperatures and thus an earlier/later solid state.

We model the transition between the magma ocean phase (phase 2) and the solid-state phase (phase 3) as instantaneous.

In the case of an entirely conductive core, we take the heat transport in all core layers to be conductive. We set the actual temperature gradient (Equations (8)–(9)) in Section 2.4 below) to conductive heat transport, using Earth’s mantle conductivity (Table 2). In the case of a conductive CEB layer, we assume a conductive CEB layer on top of a convecting core. The thickness of the conductive layer is calculated according to Equation (5) at the CEB solidification point. We take the heat transport only in that layer to be conductive, while the rest of the core remains convective.

2.3. Core Energy Sources

Our model includes several energy sources. The magnitude of the energies involved and the timescale on which they operate affect the state of the core and envelope. Below are the sources included in our model:

- I. *Formation.* As discussed in Section 2.1, the exact fraction of the accretion energy to be locked in the core depends on formation and is thus unknown. Therefore, we calculate evolutionary tracks for planets with different fractions of the binding energy from core formation, in the range of 0.05–0.5 E_{binding} . The lower bound of this range is calculated from the minimal energy of early Earth-like geophysical models (Noack et al. 2017), and the upper bound is an overestimation, assuming half of the impact energy is left in the core. We calculate models for values of 0.05, 0.1, 0.2, 0.3, and 0.5 E_{binding} .
- II. *Differentiation.* The core is initially of low viscosity (molten). Under this condition iron sinks to the center of the planet very efficiently (Stevenson 1990), i.e., during the early evolution. The released gravitational energy further heats the interior. We use the formalism of Solomon (1979) to add the differentiation energy to the core. We assume the iron-to-rock ratio to be Earth-like, and find the differentiation energy to be of a few percent of the binding energy. For simplicity, we add this energy at once (i.e., at $t = 0$), to the initial energy content of the core.⁶
- III. *Radioactive heating.* The decay of radioactive elements is an important heat source in rocky planetary interiors (Valencia et al. 2007). The dominant elements with half-lives in the gigayear regime are ²³⁸U, ²³⁵U, ²³²Th, and ⁴⁰K (Anders & Grevesse 1989; Nettelmann et al. 2011). We apply the radiogenic luminosity to Equation (6) (see below) by using the values of Nettelmann et al. (2011). The abundances of radioactive elements for exoplanets are unknown, but can range between 0.5 and 2.5 times the Earth ratio in solar analog stars (Unterborn et al. 2015). Therefore, we calculate for planets in this abundance range.
- IV. *Solidification (latent heat).* As the planet cools, the core changes from liquid to solid. The solidification process releases latent heat. We include the latent heat release in our model by adding it to each planetary layer that cools below the solidification temperature. We use the melting curve as provided in Appendix A.1. The rock latent heat

⁶ Since the exact time of differentiation ranges between 10^6 and 10^7 yr (ref), we calculated also for a later deposition of the differentiation energy, at $t = 10^7$ yr, and find the long-term (Gyr) evolution to be the same.

Table 1
Core Energy Sources

Sources	Energy (J kg ⁻¹)	Release Timescale (yr)
Formation ^a	3.4×10^7	0
Differentiation	3.1×10^6	0–10 ⁷
Radioactive decay ^b	2.6×10^6	10 ⁹
Solidification	6.0×10^5	at t_{solid}
Contraction ^c	5.5×10^4	self-consistent

Notes. Values are for a $5 M_{\oplus}$ planet with 10% envelope.

^a Core accretion energy, value for $E_{\text{acc}} = 0.2 E_{\text{binding}}$.

^b Earth-like abundance.

^c Automatically incorporated in model. Energy contribution is estimated.

of $6 \times 10^5 J \text{ kg}^{-1}$ (Morschhauser et al. 2011) is added to the luminosity (Equation (6)) of each solidified layer.

V. *Core contraction.* The pressures in sub-Neptune interiors can reach GPa levels, where core compression may heat the core and affect the thermal evolution (Mordasini et al. 2012). In our calculation, this effect is automatically included since the heavy element core is part of the evolution structure matrix, and the pressure–temperature–density relation are derived from the rock equation of state (EOS; Vazan et al. 2013). The estimate of the energy from core contraction (by $p\Delta V$) is found to be on the order of 10^4 – $10^5 J \text{ kg}^{-1}$ for a sub-Neptune mass range.

Estimates of the above energy sources and their release timescales, for a $5 M_{\oplus}$ planet with 10% envelope, appear in Table 1. The fits for the energy flux are implemented in the model by using the method described in Vazan et al. (2018). Collecting these effects, the luminosity in the core is taken to be

$$L_{\text{core}} = M_c \left(c_v \frac{dT_c}{dt} + \frac{E_{\text{radio}}}{\tau_r} e^{-(t/\tau_r)} + \frac{E_{\text{solid}}}{\Delta t} \delta(T - T_{\text{solid}}) \right), \quad (6)$$

where c_v is the specific heat capacity, M_c the core mass, and t the time. dT_c/dt describes the release of initial energy from formation and differentiation, E_{radio} and τ_r are adjusted to fit the heat production by radioactive decay as in Nettelmann et al. (2011), and E_{solid} is the solidification (latent) energy (Morschhauser et al. 2011) released on a time interval Δt , when the temperature reaches the solidification temperature ($T = T_{\text{solid}}$). The parameter values appear in Table 2. External core energy sources, such as late planetesimal capture (Chatterjee & Chen 2018), are not included in the model.

2.4. Thermal Evolution

The evolution is modeled by a 1D hydrostatic planetary code that solves the structure and evolution equations for the entire planet on one grid (see Kovetz et al. 2009; Vazan et al. 2013, 2015 for details). We use an EOS for hydrogen, helium (Saumon et al. 1995), and rock, as described in Vazan et al. (2013). The thermodynamic properties of the core (such as density, entropy, etc.) are modeled by the EOS of one material (SiO₂) as a simplification for the full mineralogy of a core.

Table 2
Model Parameters

Parameter	Value	Unit	References
E_{radio} (Equation (6))	2.64×10^{10}	erg g ⁻¹	1
τ_r (Equation (6))	1.85×10^9	yr	1
E_{solid} (Equation (6))	6×10^9	erg g ⁻¹	2
L_{\odot}	3.8515×10^{26}	W	3
κ_{op}	$Z_{\odot} - 30 \times Z_{\odot}$	cm ² g ⁻¹	4
k_{cond}	4	W m ⁻¹ K ⁻¹	5
d	0.3–1	au	
Albedo	0		

Note. Set of parameters we use in the model.

References. (1) Nettelmann et al. (2011), (2) Morschhauser et al. (2011), (3) Guenther et al. (1992), (4) Sharp & Burrows (2007), and (5) Stevenson et al. (1983).

The energy balance during the evolution is described by

$$\frac{\partial u}{\partial t} + p \frac{\partial 1}{\partial t \rho} = q - \frac{\partial L}{\partial m}, \quad (7)$$

where the symbols ρ , p , u are the density, pressure, and specific energy, respectively; q is the contribution by the additional energy sources; and m and L are the planetary mass and luminosity.

The temperature profile is determined by the heat transport rate according to

$$\frac{\partial \ln T}{\partial m} = \nabla \frac{\partial \ln p}{\partial m}. \quad (8)$$

In convective regions, the actual temperature gradient ∇ is the adiabatic temperature gradient ∇_A ; otherwise, heat transfers via radiation (in the envelope) and conduction (in the core), i.e., $\nabla = \nabla_R$, where

$$\nabla_R = \frac{\kappa_{\text{op}} L}{4\pi c G m} \frac{p}{4p_R}. \quad (9)$$

κ_{op} is the harmonic mean of the radiative and conductive opacities, and p_R is the radiation pressure.

2.4.1. Atmospheric Conditions

The atmosphere opacity regulates the planet luminosity and the contraction of the envelope. We use Rosseland mean of the radiative opacity by Sharp & Burrows (2007) for solar-metallicity grain-free atmosphere. Envelopes of sub-Neptunes may have an enhanced atmospheric metallicity from their formation (Fortney et al. 2013; Thorngren et al. 2016). Moreover, extended clouds in sub-Neptune atmospheres (e.g., Bean et al. 2011; Désert et al. 2011) indicate large atmospheric metallicities and a large opacity (Morley et al. 2013). Because of the important role of atmospheric opacity on the cooling rate of planets, we tested the sensitivity of our results to higher ($30\times$ solar) atmospheric metallicity.

At the atmospheric boundary, which is taken to be the planetary photosphere, the outer boundary condition is $\kappa_{\text{op}} p = \tau_s g$, where $g = GM/R^2$ is the gravitational acceleration, and τ_s is the optical depth of the photosphere. The envelope mass is constant during the evolution, i.e., no evaporation or gas accretion is included in the model.

2.4.2. Irradiation

We assume the temperature distribution in a gray, plane-parallel atmosphere, with a constant net outward flux F and irradiation temperature T_{irr} , to be

$$\sigma T^4(\tau) = \left(\frac{3}{4}\tau + \frac{1}{4} \right) F + g(\tau)\sigma T_{\text{irr}}^4. \quad (10)$$

where $g(\tau) = \frac{3}{2} \left(1 - \frac{1}{2}e^{-\tau} \right)$ (Kovetz et al. 1988) and σ is Stefan–Boltzmann’s constant. The temperature distribution is calculated for a vertical (maximal) irradiation flux, with no angle dependency of the incident flux (Guillot 2010). At the photosphere, where $\tau = \tau_S = 1$, the net outward luminosity of the planet is

$$L = 4\pi R^2 F = 4\pi R^2 \sigma [T^4 - g(\tau_S)T_{\text{irr}}^4]. \quad (11)$$

The irradiation temperature as a function of the distance from the star is

$$T_{\text{irr}} = \left(\frac{L_\star(1 - A)}{16\pi\sigma d^2} \right)^{1/4}, \quad (12)$$

where L_\star is the stellar luminosity (we use $L_\star = L_\odot$), d is the distance of the planet from the star, and A is the albedo. In order to separate the core effects from the environmental thermal effects, we first take $d = 1$ au as our standard model. This corresponds to the outer edge of *Kepler*’s detection region. Next, we test closer-in cases of $d = 0.3$ au and examine the effect on the results. We avoid planets at $d < 0.3$ au, from which photoevaporation can become significant, since photoevaporation by the parent star removes (part of) the gaseous envelope (Owen & Wu 2013, 2016) and thus changes the envelope mass in time.

The albedo strongly depends on the atmospheric composition and is an unknown parameter for sub-Neptunes. Here we take all the irradiation to be absorbed by the planet ($A = 0$), which is the upper bound of the irradiation effect. Thus, a non-zero-albedo planet should be located closer in for an equivalent irradiation flux.

3. Results

3.1. Magma Ocean Phase

3.1.1. Role of Core Energy Sources

In Figure 2, we show the evolution of $5 M_\oplus$ planets with 90% ($4.5 M_\oplus$) core surrounded by 10% ($0.5 M_\oplus$) hydrogen–helium envelope, located at 1 au from a Sun-like star. The radius (left) and core surface (CEB) temperature (right) are shown in the figure, where the different curves are for different approximations for core energy sources. The CEB solidification occurs when the CEB temperature crosses the dashed horizontal melting line. At this time point (which we call t_{MO}), the magma ocean phase ends. At first, all cases in the figure are modeled as in the magma ocean phase, i.e., efficient convection, even for $t > t_{\text{MO}}$. Thus, the cooling after the solidification point (thin curves) is overestimated. In Section 3.2 below, we show the effect of the solidification on the results.

The lowest core energy case (blue curve) is achieved for the lower bound of 0.5 Earth radioactive abundance and minimum initial energy from formation ($E_{\text{acc}} = 0.05E_{\text{binding}}$). Then, we increase the initial energy content of the core to 20% of the

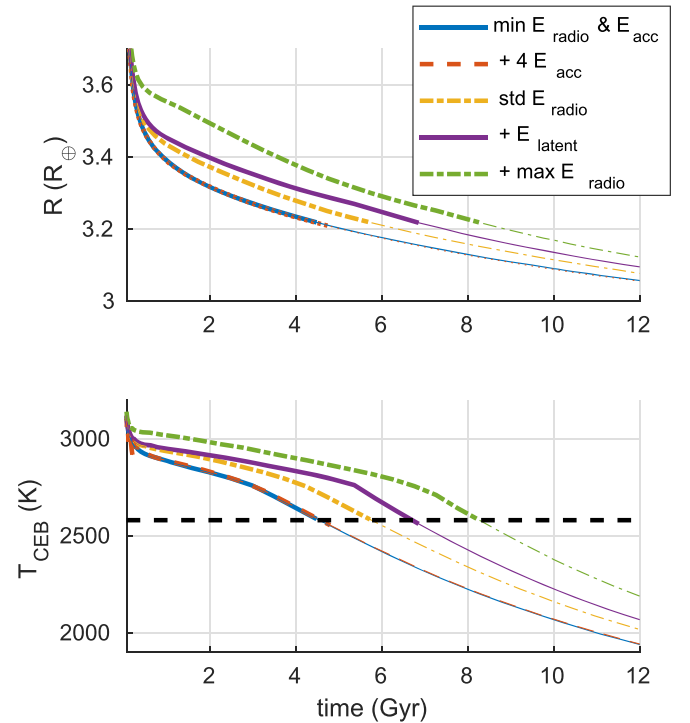


Figure 2. Radius (left) and CEB temperature (right) of $4.5 M_\oplus$ cores with a $0.5 M_\oplus$ (10%) hydrogen–helium envelope. The different radio curves are for different assumptions for core energy sources: minimal radioactive heating and low formation energy ($E_{\text{acc}} = 0.05E_{\text{binding}}$; blue), four times higher accretion energy ($E_{\text{acc}} = 0.2E_{\text{binding}}$) and including differentiation energy (red dashed), Earth ratio of radioactive heating (yellow dashed), including latent heat (blue), and maximal radioactive heating together with all previous energy sources (green dashed). The horizontal line indicates the core surface solidification.

binding energy ($E_{\text{acc}} = 0.2E_{\text{binding}}$) and include the differentiation energy (red dotted curve). As is shown in the figure, the long-term evolution is the same as the previous case, since this energy is being released efficiently during the magma ocean phase on a timescale of $\sim 10^7$ yr. Although the initial core energy content does not affect the long-term evolution, this initial energy can expand the envelope until it is no longer bound to the planet. We test this idea (see Appendix A.2) for the planets in Figure 2, and find that for an initial energy of more than 30% of the binding energy, part of the envelope is being lost.

Next, we increase the contribution from radioactive element decay to levels similar to Earth (dashed yellow). Since the radioactive energy is being released on a gigayear timescale, the long-term radius and CEB temperature are higher for this case. In the next case (purple), we added the latent heat by core solidification. The latent heat release by core solidification occurs from inside out. This is a gradual process during the magma ocean phase, which ends when the CEB solidifies, and it delays somewhat the CEB solidification by up to 1 Gyr and slightly increases the radius. This case (purple curve) of a core with Earth abundance of radioactive content and a latent heat release at solidification is our standard model.

Finally, we considered a model with radioactive levels enhanced by a factor of 2.5 over Earth. This high radioactive level is motivated by the maximal measured abundance around Sun-like stars (Unterborn et al. 2015). This enhanced radioactive heating (dashed green) in the core is found to be the most important energy contribution to the long-term evolution. Variation in the fraction of radioactive elements in the observed

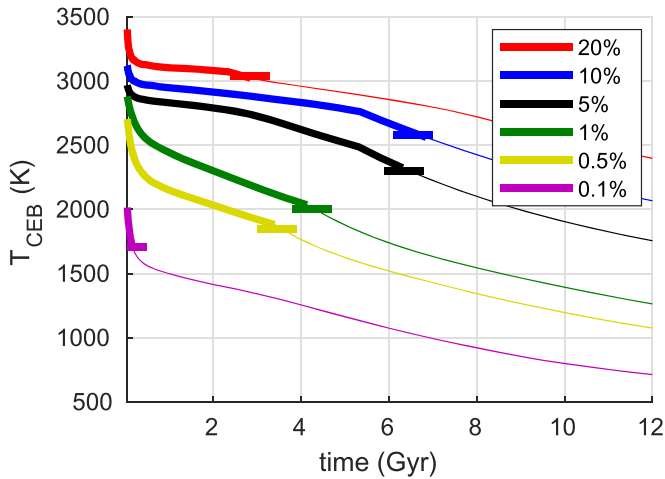


Figure 3. CEB temperature of $4.5 M_{\oplus}$ cores with different envelope masses. The percentages denote the mass fractions of the envelope with respect to the total planet mass. The horizontal lines indicate the (pressure-dependent) CEB solidification temperature of each planet (see Appendix A.1). The evolution is modeled by efficient magma ocean cooling, which overestimates the cooling after solidification (thin curves).

range of $0.5\text{--}2.5\times$ Earth abundance, results in up to a 5% radius change for planets with a solar-metallicity envelope. In general, the fraction of radioactive elements and solidification (latent) heat are the most significant core energy sources for the long term. In addition to inflating the radius, the excess heat delays the CEB solidification time (from 4 to 8 Gyr in this case), and thus prolongs the magma ocean phase. For these cases, many observed sub-Neptunes are likely to be in a magma ocean phase.

3.1.2. Dependence on the Envelope Mass

In Figure 3, we follow the change in surface (CEB) temperature during the evolution of planets with the same core mass surrounded by envelopes of different masses. We use the $4.5 M_{\oplus}$ standard core model (purple curve in Figure 2) and vary the mass of the envelope between 0.1% and 20% ($0.005\text{--}1 M_{\oplus}$). The horizontal curves in the figure show the point when the CEB solidifies for the surface pressure and temperature of this planet, as described in Appendix A.1. In these runs, as before, magma ocean phase conditions are assumed for the entire evolution, thus the cooling after solidification (thin curves) is overestimated.

As is shown in the figure, the magma ocean phase (the thick part of each curve) for planets with significant envelopes lasts much longer than in the case of Earth. As the atmospheric mass increases, the temperature on the surface of the core is higher, and as a result, the surface stays molten for a longer time. Therefore, for most of the cases in Figure 3, the duration of the magma ocean phase increases with envelope mass.

However, with increasing envelope mass, the pressure on the planet surface also increases and so does the melting temperature. For a thick envelope of about $1 M_{\oplus}$ (red curve), the melting temperature is above 3000 K and therefore the CEB solidifies earlier than for lower mass envelopes. As a result, the magma ocean duration is limited to up to several gigayears, since for high-mass envelopes ($>0.5 M_{\oplus}$), the required higher melting temperatures shorten the magma ocean phase. We find that sub-Neptune planets with envelope masses between $0.01 M_{\oplus} < M_{\text{env}} < 1 M_{\oplus}$ make the transition from magma ocean to solidified state during the time we observe them

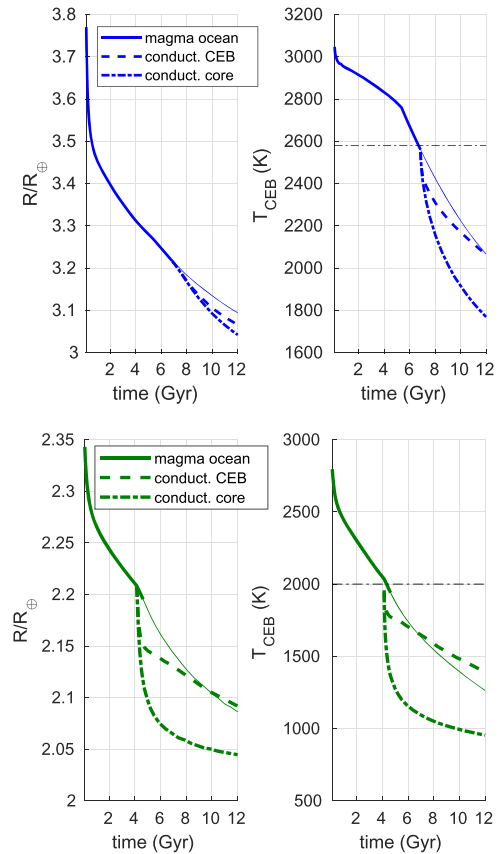


Figure 4. Radius (left) and CEB temperature (right) for a $4.5 M_{\oplus}$ core with an envelope. Top panels: 10% envelope mass ($0.5 M_{\oplus}$); bottom panels: 0.1% envelope mass ($0.005 M_{\oplus}$). The solid curve is for efficient core cooling (magma ocean). The evolution with a conductive CEB layer (dashed) and with a conductive core (dashed-dotted) are shown after the CEB reaches the solidification temperature (horizontal dashed).

(1–7 Gyr). In the next section, we estimate the effect of such a transition on the properties of the planet.

3.2. Solid-state Phase

In Figure 4, we present the planetary radius (left) and the CEB temperature (right) for a $4.5 M_{\oplus}$ core with $0.5 M_{\oplus}$ (10%) and $0.05 M_{\oplus}$ (1%) envelopes. The solid curves represent the efficient core cooling as in the magma ocean phase (same as the blue and green curves in Figure 3). After the CEB solidifies (dashed horizontal temperature line), we calculate for the two scenarios described in Section 2.2 the thermal evolution with an entirely conductive core (dashed-dotted) and the thermal evolution with a conductive CEB layer (dashed). The thickness of the conductive layer, according to Equation (5), is about 100 km, and the timescale for cooling by conduction through this layer is on the order of 10^8 yr.

As is shown in the figure, the CEB temperature rapidly changes at the point where the model (suddenly) assumes a conductive structure. The conductive CEB scenario moderates the flux from the core but keeps the long-term surface temperature similar to the magma ocean case. The conductive boundary layer acts as a bottleneck for the cooling, but it is not thick enough to slow the cooling substantially. In the conductive core scenario, the cooling is much slower; heat is locked in the core while the surface temperature drops.

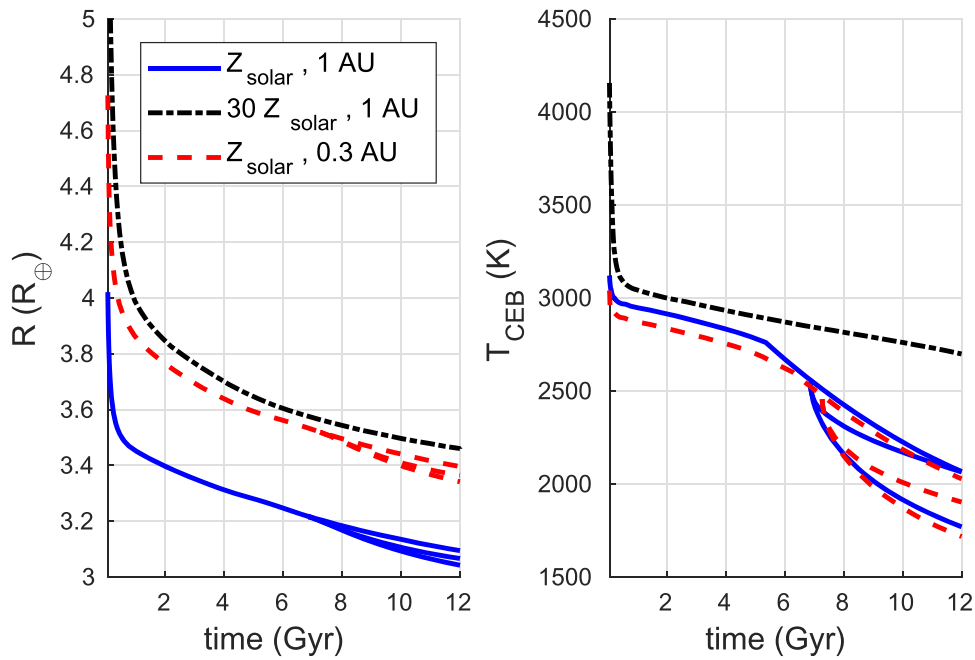


Figure 5. Radius (left) and CEB temperature (right) for $5 M_{\oplus}$ planets with a $0.5 M_{\oplus}$ (10%) envelope. The different curve styles are for different envelope conditions: standard case of solar-metallicity opacity located at 1 au (solid blue), planet with enhanced atmospheric opacity of $30\times$ solar (dashed–dotted black), and planet with a higher irradiation located at 0.3 au (dashed red). The different curves of each color represent the different core-cooling scenarios after core solidification (phase 3).

The effect of solidification on the thermal evolution depends on the envelope mass. In the case of the $0.5 M_{\oplus}$ envelope (upper panels), the CEB solidification occurs at a later time than in the $0.05 M_{\oplus}$ envelope case. At a later time, the core energy budget is smaller (mainly due to radioactive decay). In addition, the cooling at the bottom of the thicker envelope (the core interface) is slower. Therefore, the drop in CEB temperature is more moderate.

While the effect of the core properties is significant for some of the cases, the effect on the radius is more limited. The maximum radius change for sub-Neptune planets in our sample resulting from solidification is about 6%, or $0.1 R_{\oplus}$. This maximum is achieved for a planet with a $0.05 M_{\oplus}$ envelope (bottom left in Figure 4). For planets with lower mass envelopes, the contribution of the envelope to the total radius is small. On the other hand, planets with high envelope masses, such as the $0.5 M_{\oplus}$ envelope case (upper left in Figure 4), have lower core-to-envelope mass ratios and smaller energy contents at solidification, which limit the effect on the radius.

3.3. Envelope Conditions and Planet Mass

Since the overall thermal evolution of the core depends also on the thermal evolution of the envelope, the thermal properties of the envelope are expected to change the results. Therefore, we calculate for enhanced ($30\times$ solar) atmospheric opacity and higher irradiation by the star ($d = 0.3$ au). In Figure 5, we show the radius (left) and CEB temperature (right) in time for identical planets with different atmospheric conditions. The standard case (blue) is compared to a case with enhanced opacity (dashed–dotted) and to a case with stronger irradiation (dashed). Additional representative results appear in Table 3. As is shown in the figure, irradiation has a significant effect on the envelope radius,⁷ within

⁷ Irradiation extends the outer atmosphere. Since our evolution model is calculated for a fixed mass, we verify that the outermost layer is at $p > 10$ millibar, to avoid “fake” radii by extension of the outermost layers.

the range of previous works (Lopez & Fortney 2014; Howe & Burrows 2015). However, irradiation does not change the surface conditions for significant envelope masses ($>0.01 M_{\oplus}$). As the outer layers of the envelope expands by irradiation, the conditions at the bottom of the envelope remain similar to the standard case. Thus, the location of the planet (for $d > 0.3$ au) has a small effect on the core evolution in the presence of a significant envelope (photoevaporation is not included in the model).

Atmospheric opacity, on the other hand, changes both the radius and the core surface temperature substantially. In the enhanced opacity case, the envelope cooling is slower. Thus, the envelope traps the heat from the core and delays the core cooling. As is shown in Figure 5, a metallicity of $30\times$ solar keeps the core surface hotter (molten) for a much longer time than in the standard case. In the case of a lower mass envelope, like for example a $4.5 M_{\oplus}$ core with 0.1% envelope, the enhanced atmospheric metallicity ($30\times$ solar) delays the surface solidification from less than 0.5 Gyr to more than 2 Gyr. Moreover, the effect of core thermal properties on the radius becomes more important for high atmospheric opacity. Uncertainty in radioactive elements, in the range of 0.5–2.5 Earth ratio, results in up to a 15% radius change for planets with enhanced envelope metallicity, in comparison to only 5% for similar planets with solar metallicity.

We also vary the mass of the core by a factor of 2 ($2.25 M_{\oplus}$ and $9 M_{\oplus}$) for different envelope masses (examples in Table 3). We find that cores of different masses with the same envelope mass result in similar cooling rates of the core surface,⁸ i.e., the envelope mass, and not the envelope fraction, is the key parameter driving the core thermal evolution. The reason is that during the magma ocean phase, the pressure–temperature conditions at the bottom of the envelope are determined by the adiabatic structure of the envelope. Hence, the same envelope

⁸ It should be noted that modification of the core heat transport by the change in mass (e.g., Stamenković et al. 2012) is not included in our simplified model.

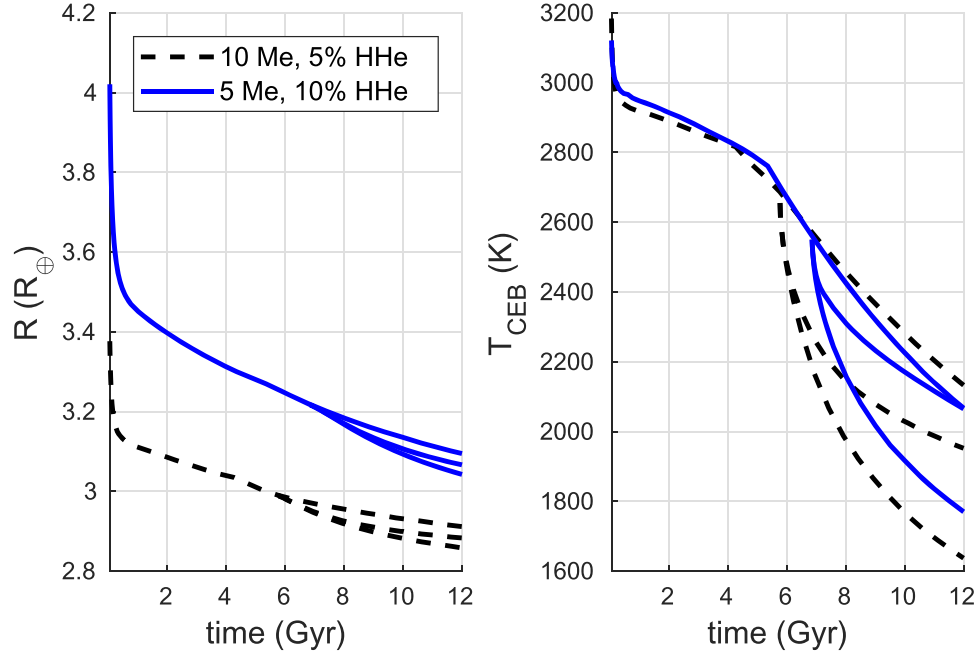


Figure 6. Radius (left) and CEB temperature (right) for $10 M_{\oplus}$ (dashed black) and $5 M_{\oplus}$ (solid blue) planets with the same envelope mass of $0.5 M_{\oplus}$. The different curves of each planet represent the different core cooling scenarios after solidification (phase 3). The cores feature a similar thermal evolution until solidification.

Table 3
Parameter Study

Model	M_{core}	M_{env}		t_{MO} (Gyr)	1 Gyr	Radius (R_{\oplus})	10 Gyr
$4.5 M_{\oplus}$	$0.5 M_{\oplus}$	std		$6.8^{+1.5}_{-2.3}$	$3.45^{+0.11}_{-0.07}$	$3.28^{+0.06}_{-0.08}$	$3.14^{+0.03}_{-0.05}$
		$\kappa_{\text{op}} (30 \times Z_{\oplus})$		>13	$4.00^{+0.21}_{-0.12}$	$3.71^{+0.06}_{-0.12}$	$3.50^{+0.04}_{-0.04}$
		$d (0.3 \text{ au})$		$6.9^{+2}_{-2.2}$	$3.86^{+0.18}_{-0.1}$	$3.60^{+0.08}_{-0.09}$	$3.44^{+0.04}_{-0.05}$
$4.5 M_{\oplus}$	$0.05 M_{\oplus}$	std		$4.6^{+1.4}_{-2.4}$	$2.26^{+0.05}_{-0.03}$	$2.19^{+0.03}_{-0.08}$	$2.10^{+0.02}_{-0.06}$
		$\kappa_{\text{op}} (30 \times Z_{\oplus})$		>13	$2.45^{+0.07}_{-0.03}$	$2.36^{+0.07}_{-0.03}$	$2.27^{+0.06}_{-0.0}$
		$d (0.3 \text{ au})$		$4.6^{+1.2}_{-1.9}$	$2.44^{+0.09}_{-0.01}$	$2.33^{+0.07}_{-0.02}$	$2.24^{+0.04}_{-0.01}$
$4.5 M_{\oplus}$	$0.005 M_{\oplus}$	std		$0.2^{+0.4}_{-0.05}$	$1.92^{+0.02}_{-0.07}$	$1.88^{+0.02}_{-0.05}$	$1.85^{+0.01}_{-0.03}$
		$\kappa_{\text{op}} (30 \times Z_{\oplus})$		$2.4^{+1.8}_{-1.1}$	$2.04^{+0.05}_{-0.04}$	$1.96^{+0.03}_{-0.03}$	$1.93^{+0.01}_{-0.02}$
		$d (0.3 \text{ au})$		$0.4^{+1.2}_{-0.1}$	$2.04^{+0.03}_{-0.03}$	$1.98^{+0.02}_{-0.02}$	$1.96^{+0.01}_{-0.02}$
$2.25 M_{\oplus}$	$0.05 M_{\oplus}$	std		$3.5^{+1.7}_{-1.9}$	$2.39^{+0.06}_{-0.07}$	$2.20^{+0.06}_{-0.04}$	$2.07^{+0.03}_{-0.04}$
		$\kappa_{\text{op}} (30 \times Z_{\oplus})$		$11.4^{+1.6}_{-1.4}$	$2.89^{+0.2}_{-0.2}$	$2.53^{+0.13}_{-0.06}$	$2.41^{+0.04}_{-0.04}$
		$d (0.3 \text{ au})$		$3.2^{+2.1}_{-1.4}$	$2.86^{+0.14}_{-0.13}$	$2.54^{+0.13}_{-0.07}$	$2.39^{+0.04}_{-0.03}$
$2.25 M_{\oplus}$	$0.005 M_{\oplus}$	std		$0.2^{+0.6}_{-0.2}$	$1.82^{+0.03}_{-0.06}$	$1.72^{+0.03}_{-0.04}$	$1.68^{+0.01}_{-0.03}$
		$\kappa_{\text{op}} (30 \times Z_{\oplus})$		$3.5^{+1.3}_{-1.7}$	$2.05^{+0.07}_{-0.11}$	$1.87^{+0.04}_{-0.04}$	$1.82^{+0.01}_{-0.03}$
		$d (0.3 \text{ au})$		$0.8^{+0.8}_{-0.3}$	$2.06^{+0.04}_{-0.8}$	$1.92^{+0.04}_{-0.02}$	$1.88^{+0.01}_{-0.02}$
$9 M_{\oplus}$	$1 M_{\oplus}$	std		$0.1^{+0.01}_{-0.03}$	$3.58^{+0.07}_{-0.03}$	$3.44^{+0.06}_{-0.03}$	$3.36^{+0.02}_{-0.02}$
		$\kappa_{\text{op}} (30 \times Z_{\oplus})$		$3.7^{+1.9}_{-1.6}$	$3.96^{+0.1}_{-0.04}$	$3.71^{+0.06}_{-0.04}$	$3.6^{+0.04}_{-0.02}$
		$d (0.3 \text{ au})$		$0.1^{+0.03}_{-0.01}$	$3.78^{+0.11}_{-0.05}$	$3.6^{+0.06}_{-0.03}$	$3.52^{+0.02}_{-0.03}$
$9 M_{\oplus}$	$0.5 M_{\oplus}$	std		$5.3^{+1.4}_{-2.4}$	$3.11^{+0.05}_{-0.04}$	$3.02^{+0.02}_{-0.05}$	$2.93^{+0.03}_{-0.03}$
		$\kappa_{\text{op}} (30 \times Z_{\oplus})$		>13	$3.38^{+0.09}_{-0.06}$	$3.22^{+0.05}_{-0.05}$	$3.12^{+0.03}_{-0.02}$
		$d (0.3 \text{ au})$		$5.7^{+1.4}_{-2.2}$	$3.27^{+0.07}_{-0.07}$	$3.13^{+0.04}_{-0.05}$	$3.06^{+0.01}_{-0.03}$

Note. Planet radii and the duration of the magma ocean phase (t_{MO}) for various planets. Results are given for the standard (std) core model (blue curve in Figures 2–4), the high atmosphere opacity model (κ_{op}), and the close-in model ($d = 0.3 \text{ au}$). Error bars indicate the variation of t_{MO} and radius resulting from the variation in core properties (as in Figure 2). For $t > t_{\text{MO}}$, radius error bars include the solid-state phase.

mass leads to similar pressure–temperature conditions at the core surface. In Figure 6, we show this trend for two planets with different total masses but the same envelope mass: the

difference in magma ocean duration (CEB temperature) between a $10 M_{\oplus}$ planet with 5% envelope and a $5 M_{\oplus}$ planet with 10% envelope (same envelope mass) is smaller than the

uncertainty within the core thermal properties for each planet. While the two cores feature similar thermal evolution until solidification, the solidification point is somewhat different. The $10 M_{\oplus}$ planet reaches CEB solidification earlier than the $5 M_{\oplus}$ planet because of higher surface pressure, which increases the melting (solidification) temperature. The radii of the $5 M_{\oplus}$ planet is larger because of irradiation effect on cores with lower gravity (e.g., Lopez & Fortney 2014). Conversely, the higher (lower) solidification temperature for more (less) massive cores, due to surface pressures, and the sensitivity to thermal effects by the higher (lower) gravity are found to have only small effects on the radius variation by the core properties. Also here, high atmospheric opacity intensifies the core thermal effects.

4. Discussion

Our results indicate that many of the observed sub-Neptune planets are in the magma ocean phase for several gigayears. This is very different from the short magma ocean phase of planets in our solar system (e.g., Elkins-Tanton 2012). Because of its prolonged existence, it is likely that the core and envelope interact strongly, not only regarding their thermal properties (as modeled here) but also regarding their composition. For example, the solubility of the envelope hydrogen in the silicate melt (Hirschmann et al. 2012) can be significant for high temperature and pressure conditions as in sub-Neptunes (Chachan & Stevenson 2018). Consequently, sub-Neptune planets with a less than $1 M_{\oplus}$ envelope may contain a significant fraction of volatiles in their cores, which affects the rock thermal and physical properties.

Conversely, the long interaction of the molten convective core with the hydrogen envelope may also enrich the envelope with metals from the molten core. Currently, there is a lack of knowledge (experimental data as well as modeling) of the rock–envelope interaction for sub-Neptune conditions. Most of the current knowledge pertains to processes on Earth-like terrestrial planets (e.g., Abe & Matsui 1986; Hirschmann 2012). Studies of rock–envelope interaction for sub-Neptune pressure–temperature conditions are necessary to improve our understanding of the structure and thermal properties of these objects.

As we show in this work, the envelope mass determines the state and the cooling rate of the core. *Kepler*’s data reveal a statistical dip in planetary radius between the two peaks of $1.3 R_{\oplus}$ and $2.6 R_{\oplus}$ (Fulton et al. 2017). This valley, which divides the close-in planets into two populations, can be a result of envelope mass loss by photoevaporation (Owen & Wu 2017; Jin & Mordasini 2018). Envelope mass loss during the evolution shortens the magma ocean phase (as long as $t_{\text{evap}} < t_{\text{MO}}$) and thus affects the thermal evolution of the core. Thus, the valley actually divides the planets also into two thermal populations, where the radius peak of $1.3 R_{\oplus}$ is for bare (solid state) cores, and the $2.6 R_{\oplus}$ peak is for magma ocean phase cores ($M_{\text{env}} > 0.05 M_{\oplus}$). Future studies of magma–envelope chemical interaction can provide atmospheric markers to be detected in order to distinguish between the two populations.

This study is focused on sub-Neptune planets around a Sun-like star (G-type). Sub-Neptune planets around M-type stars, which appear to be common (e.g., Mulders et al. 2015), may have a different formation environment (e.g., Kennedy & Kenyon 2008; Ormel et al. 2017) and thus a different core

thermal contribution. For example, different core formation timescales in a lower mass disk will change the formation energy left in the core. Moreover, a low-mass disk may have a different composition. As a result, the differentiation energy, which is derived from the iron-to-rock ratio, will change. The radioactive element abundances and the rock latent heat, which we find to contribute the most to the planet’s long-term evolution, are derived from the rock mineralogy, which depends on metals abundances and thermal conditions of the building blocks in the disk. As a result, the (Earth-like) values for the core energy sources we used in this work (Section 2.3) will change for M-type stars.

This work considers rocky cores, without any fraction of ice. Ice-rich cores have substantial effects on both radius–mass relation and atmospheric properties (Chen & Rogers 2016). However, during the solidification of the molten core, water would be expelled from the core (e.g., Elkins-Tanton 2008). For the planetary and envelope mass range of sub-Neptunes, water is found to stay in the envelope in vapor form; the surface pressure–temperature conditions do not allow for liquid water for the parameter range we studied here. As we show in Figure 3, envelope mass larger than $0.02 M_{\oplus}$ keeps the surface temperature above 1000 K for more than 10 Gyr. Thus, if the core contains some fraction of ice, the envelope is presumably saturated with vapor and thus denser than the H/He envelope in our model. In this case, the increase in core radius by the icy (lighter) materials diminishes due to the decrease in envelope radius because of the higher mean molecular weight. Moreover, ice-rich cores are expected to contain less radioactive elements, which are scaled with the rocky part. Therefore, the core energy source of radioactive heating is reduced.

Close-in planets usually have low envelope masses and thus exhibit limited radius change due to core thermal contribution, as is discussed in Section 3.2. However, for close-in planets, additional mechanisms that are not included in our model can affect the contribution of the core to the overall thermal evolution: (1) photoevaporation by the parent star. The early released core energy (formation and differentiation) extends the envelope radius and hence accelerates photoevaporation. Photoevaporation is expected to reduce the envelope mass and therefore shorten the magma ocean phase duration. Including photoevaporation simulation (e.g., Murray-Clay et al. 2009) in the core–envelope evolution model is essential for modeling of close-in planets, and we would like to address it in a future work. (2) Close-in planets experience tidal forces from the parent star. Tidal heating is a continuous energy source in the core, but may not be significant for super-Earth cores (Efroimsky 2012). (3) Late planetesimal capture can add energy during the planet’s evolution, as well as increase the atmospheric metallicity. This contribution is relevant in particular for planets less massive than $10 M_{\oplus}$ and with envelope mass fractions less than 10% (Chatterjee & Chen 2018).

The core model that appears in this work is a first-order estimate for core thermal evolution. In detailed (envelope-less) geophysical models (e.g., van den Berg et al. 2019), the transfer between the different core thermal phases is continuous, and the heat transport depends on thermal and physical properties of the core minerals. As we show here, the core–envelope thermal effects are mutual, i.e., the envelope changes the core thermal state in time. Thus, in order to improve the existing sub-Neptune models, one should link the geophysical core

model to envelope thermal evolution. Such a combined model is challenging because of its self-dependent nature, but is necessary in order to better understand the interiors of sub-Neptune planets.

5. Conclusion

We have modeled the thermal evolution of sub-Neptune planets with core and hydrogen–helium envelope on one structure grid. Our model divides the evolution of the core into three phases: initial (formation phase), efficient cooling (magma ocean phase), and inefficient cooling (solid-state phase). We have examined the contribution of the core energy sources to the thermal evolution of the planet as a whole. In particular, we followed the mutual core–envelope thermal effects on the core solidification and the planet radius evolution.

We summarize our main conclusions below:

1. Most of the observed sub-Neptune planets are in the magma ocean phase (molten surface). We find that the duration of the magma ocean phase for planets with envelope masses between $0.01 M_{\oplus}$ and $1 M_{\oplus}$ lies between 1 and 7 Gyr.
2. Because of its efficient cooling, the magma ocean phase renders the evolution insensitive to the initial conditions. For this reason, the initial thermodynamic state of the core (heat of formation and iron differentiation) does not influence the radius evolution for more than several 10^7 yr.
3. Radioactive decay is the most significant energy source to affect the planet radius, and the latent heat from solidification is the second. In the long term, the planet radius variation as a result of uncertainty in these core energy sources is at most 15%.
4. After solidification of the CEB, the heat flux from the core decreases further. We calculate that the variation in radius due to uncertainties regarding the post-solidification phase is no larger than 6%.
5. Overall, for typical model parameters, the contribution from the thermal state of the core to the planet radius is rather limited (a few percent at most). Therefore, the inferred envelope mass from the mass–radius relation is mostly proportional to the envelope (H/He) mass fraction.
6. The atmospheric opacity significantly prolongs the magma ocean phase and amplifies the core effects on the envelope evolution. Irradiation (for $d > 0.3$ au), on the other hand, has only a minor effect on the core evolution.

We thank Dave Stevenson, Wim van Westrenen, and Arie van den Berg for useful comments and discussions. A.V. thanks Attay Kovetz for helpful ideas for code modifications. A.V. acknowledges support by the Amsterdam Academic Alliance (AAA) Fellowship and by the Netherlands Origins Center. C.W.O. is supported by the Netherlands Organization for Scientific Research (NWO; VIDI project 639.042.422).

Appendix

A.1. Rock Melting Curve

To calculate the rock melting curve, we use the solidus and liquidus pressure–temperature relations as follows: for pressures below 10 GPa, we take melting curves for peridotite,

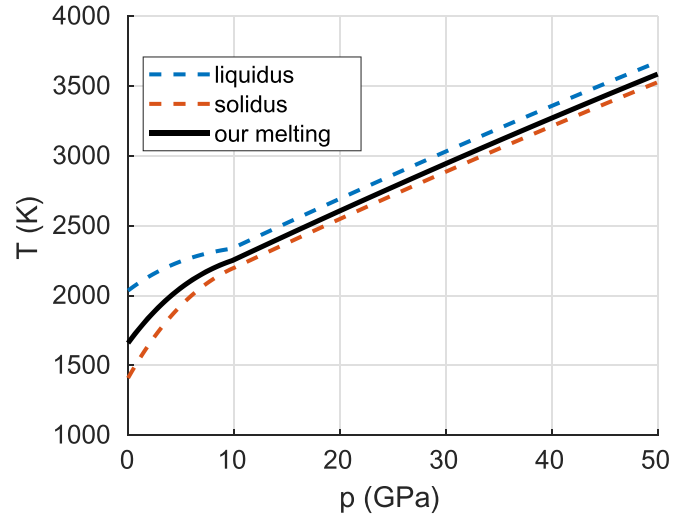


Figure 7. Rock melting curve we use in this work to determine the rocky core solidification. We define our melting curve (solid black) at 40% between the solidus (red dashed) and liquidus (blue dashed). See Appendix A.1 for details.

based on de Smet et al. (1999) and consistent with melting profiles from Hirschmann (2000; see also Noack et al. 2017):

$$T_{\text{solid}} = 1409.15 \text{ K} + 134.2 p - 6.581 p^2 + 0.1054 p^3$$

$$T_{\text{liquid}} = 2035.15 \text{ K} + 57.46 p - 3.487 p^2 + 0.0769 p^3$$

For pressures above 10 GPa we use melting curves for perovskite, based on Stamenković et al. (2011) for the solidus. We use a fixed difference between solidus and liquidus due to lack of experimental data:

$$T_{\text{solid}} = 1835 \text{ K} + 36.918 p - 0.065444 p^2 + 0.000076686 p^3 - 3.09272 \times 10^{-8} p^4$$

$$T_{\text{liquid}} = 1980 \text{ K} + 36.918 p - 0.065444 p^2 + 0.000076686 p^3 - 3.09272 \times 10^{-8} p^4$$

We define our melting curve at 40% between the solidus and liquidus. We assume that up to 40% melt, the rock behaves like a solid, and above that as a magma ocean. Thus, the critical melting temperature that we use as a transition between a rock behaving as a solid and a rock behaving as a liquid is

$$T_{\text{melt}} = 1659.55 \text{ K} + 103.504 p - 5.3434 p^2 + 0.094 p^3$$

for $p < 10$ GPa, and

$$T_{\text{melt}} = 1893 \text{ K} + 36.918 p - 0.065444 p^2 + 0.000076686 p^3 - 3.09272 \times 10^{-8} p^4$$

for $p > 10$ GPa. In Figure 7, we show the resulting rock melting temperature as a function of the CEB pressure for the range of sub-Neptune planets.

A.2. Envelope Mass Loss

As we show in Section 3, the initial core energy content does not affect the long-term radius evolution. However, this energy can bloat the envelope until it is no longer bound to the planet (Ginzburg et al. 2016, 2018). Here, we test this idea by adding high fractions of the formation core binding energy to the early phase core, and following the radius of the planet in comparison to its Hill radius. The expansion of the envelope is an outcome of

the self-consistent core and envelope thermal evolution, accounting for the core heat flux and cooling, material properties (e.g., tabular EOSs and opacity), and their time dependency. We find that part of the envelope is being lost ($R_p > R_{\text{Hill}}$) when high fractions of formation energy is initially stored in the core. As the envelope expands from the core luminosity, the inner part of the envelope remains gravitationally bound to the core, and later on it cools more efficiently (than a thick envelope) and contracts. What fraction of the envelope is removed depends mainly on the initial core energy content, atmospheric opacity profile, and the distance from the star (Hill sphere). Under the conditions of our model, we find that envelope loss due to core energy starts when more than 30% of the accretion energy remains in the core after its formation. For a core energy content of 40%, for example, our standard model of $4.5 M_{\oplus}$ core cannot retain more than a $0.1 M_{\oplus}$ envelope. If less than 20% of the core binding energy is left in the core after its formation, all the planetary envelopes within the range of this work survive.

ORCID iDs

A. Vazan  <https://orcid.org/0000-0001-9504-3174>

C. Dominik  <https://orcid.org/0000-0002-3393-2459>

References

- Abe, Y., & Matsui, T. 1986, *JGR*, **91**, E291
- Anders, E., & Grevesse, N. 1989, *GeCoA*, **53**, 197
- Baraffe, I., Chabrier, G., & Barman, T. 2008, *A&A*, **482**, 315
- Batalha, N. M., Rowe, J. F., Bryson, S. T., et al. 2013, *ApJS*, **204**, 24
- Bean, J. L., Désert, J.-M., Kabath, P., et al. 2011, *ApJ*, **743**, 92
- Chachan, Y., & Stevenson, D. J. 2018, *ApJ*, **854**, 21
- Chatterjee, S., & Chen, H. 2018, *ApJ*, **852**, 58
- Chen, H., & Rogers, L. A. 2016, *ApJ*, **831**, 180
- Coughlin, J. L., Mullally, F., Thompson, S. E., et al. 2016, *ApJS*, **224**, 12
- Désert, J.-M., Bean, J., Miller-Ricci Kempton, E., et al. 2011, *ApJL*, **731**, L40
- de Smet, J. H., van den Berg, A. P., & Vlaar, N. J. 1999, *Litho*, **48**, 153
- Efroimsky, M. 2012, *ApJ*, **746**, 150
- Elkins-Tanton, L. T. 2008, *E&PSL*, **271**, 181
- Elkins-Tanton, L. T. 2012, *AREPS*, **40**, 113
- Fortney, J. J., Mordasini, C., Nettelmann, N., et al. 2013, *ApJ*, **775**, 80
- Fulton, B. J., Petigura, E. A., Howard, A. W., et al. 2017, *AJ*, **154**, 109
- Ginzburg, S., Schlichting, H. E., & Sari, R. 2016, *ApJ*, **825**, 29
- Ginzburg, S., Schlichting, H. E., & Sari, R. 2018, *MNRAS*, **476**, 759
- Guenther, D. B., Demarque, P., Kim, Y.-C., & Pinsonneault, M. H. 1992, *ApJ*, **387**, 372
- Guillot, T. 2010, *A&A*, **520**, A27
- Guillot, T., Chabrier, G., Gautier, D., & Morel, P. 1995, *ApJ*, **450**, 463
- Hirschmann, M. M. 2000, *GGG*, **1**, 1042
- Hirschmann, M. M. 2012, *E&PSL*, **341**, 48
- Hirschmann, M. M., Withers, A. C., Ardia, P., & Foley, N. T. 2012, *E&PSL*, **345**, 38
- Howard, A. W., Marcy, G. W., Bryson, S. T., et al. 2012, *ApJS*, **201**, 15
- Howe, A. R., & Burrows, A. 2015, *ApJ*, **808**, 150
- Ikoma, M., & Hori, Y. 2012, *ApJ*, **753**, 66
- Jin, S., & Mordasini, C. 2018, *ApJ*, **853**, 163
- Jontof-Hutter, D., Ford, E. B., Rowe, J. F., et al. 2016, *ApJ*, **820**, 39
- Karato, S.-I., & Wu, P. 1993, *Sci*, **260**, 771
- Kennedy, G. M., & Kenyon, S. J. 2008, *ApJ*, **682**, 1264
- Kovetz, A., Prialnik, D., & Shara, M. M. 1988, *ApJ*, **325**, 828
- Kovetz, A., Yaron, O., & Prialnik, D. 2009, *MNRAS*, **395**, 1857
- Lopez, E. D., & Fortney, J. J. 2014, *ApJ*, **792**, 1
- Lopez, E. D., Fortney, J. J., & Miller, N. 2012, *ApJ*, **761**, 59
- Mordasini, C., Alibert, Y., Georgy, C., et al. 2012, *A&A*, **547**, A112
- Morley, C. V., Fortney, J. J., Kempton, E. M.-R., et al. 2013, *ApJ*, **775**, 33
- Morschhauser, A., Grott, M., & Breuer, D. 2011, *Icar*, **212**, 541
- Mulders, G. D., Pascucci, I., & Apai, D. 2015, *ApJ*, **814**, 130
- Murray-Clay, R. A., Chiang, E. I., & Murray, N. 2009, *ApJ*, **693**, 23
- Nettelmann, N., Fortney, J. J., Kramm, U., & Redmer, R. 2011, *ApJ*, **733**, 2
- Noack, L., Höning, D., Rivoldini, A., et al. 2016, *Icar*, **277**, 215
- Noack, L., Rivoldini, A., & Van Hoolst, T. 2017, *PEPI*, **269**, 40
- Ormel, C. W., Liu, B., & Schoonenberg, D. 2017, *A&A*, **604**, A1
- Owen, J. E., & Wu, Y. 2013, *ApJ*, **775**, 105
- Owen, J. E., & Wu, Y. 2016, *ApJ*, **817**, 107
- Owen, J. E., & Wu, Y. 2017, *ApJ*, **847**, 29
- Poirier, J.-P. 2000, *Introduction to the Physics of the Earth's Interior* (Cambridge: Cambridge Univ. Press)
- Pollack, J. B., Hubickyj, O., Bodenheimer, P., et al. 1996, *Icar*, **124**, 62
- Rogers, L. A., & Seager, S. 2010, *ApJ*, **712**, 974
- Saumon, D., Chabrier, G., & van Horn, H. M. 1995, *ApJS*, **99**, 713
- Sharp, C. M., & Burrows, A. 2007, *ApJS*, **168**, 140
- Solomon, S. C. 1979, *PEPI*, **19**, 168
- Stamenković, V., Breuer, D., & Spohn, T. 2011, *Icar*, **216**, 572
- Stamenković, V., Noack, L., Breuer, D., & Spohn, T. 2012, *ApJ*, **748**, 41
- Stevenson, D. J. 1990, in *Fluid Dynamics of Core Formation*, ed. H. E. Newsom & J. H. Jones (New York: Oxford Univ. Press), 231
- Stevenson, D. J., Spohn, T., & Schubert, G. 1983, *Icar*, **54**, 466
- Tackley, P. J., Ammann, M., Brodholt, J. P., Dobson, D. P., & Valencia, D. 2013, *Icar*, **225**, 50
- Thorngren, D. P., Fortney, J. J., Murray-Clay, R. A., & Lopez, E. D. 2016, *ApJ*, **831**, 64
- Turcotte, D. L., & Oxburgh, E. R. 1967, *JFM*, **28**, 29
- Unterborn, C. T., Johnson, J. A., & Panero, W. R. 2015, *ApJ*, **806**, 139
- Valencia, D., O'Connell, R. J., & Sasselov, D. D. 2007, *ApJL*, **670**, L45
- van den Berg, A. P., Yuen, D. A., Beebe, G. L., & Christiansen, M. D. 2010, *PEPI*, **178**, 136
- van den Berg, A. P., Yuen, D. A., Umemoto, K., Jacobs, M. H. G., & Wentzcovitch, R. M. 2019, *Icar*, **317**, 412
- Vazan, A., Helled, R., Kovetz, A., & Podolak, M. 2015, *ApJ*, **803**, 32
- Vazan, A., Kovetz, A., Podolak, M., & Helled, R. 2013, *MNRAS*, **434**, 3283
- Vazan, A., Ormel, C. W., & Dominik, C. 2018, *A&A*, **610**, L1
- Wolfgang, A., & Lopez, E. 2015, *ApJ*, **806**, 183